Colliding Clouds: The Star Formation Trigger of the Stellar Cluster Around BD+40° 4124

Leslie W. Looney[1], Shiya Wang[1], Murad Hamidouche[1], Pedro N. Safier[2,3],
and Randolf Klein[4,5]

ABSTRACT

We present BIMA and SCUBA observations of the young cluster associated with $BD + 40°$ 4124 in the dense molecular gas tracer CS $J = 2 \rightarrow 1$ and the continuum dust continuum at $\lambda = 3.1$ mm and $\lambda = 850$ μm. The dense gas and dust in the system is aligned into a long ridge morphology extending $\sim$0.4 pc with 16 gas clumps of estimated masses ranging from 0.14 - 1.8 $M_\odot$. A north-south variation in the CS center line velocity can be explained with a two cloud model. We posit that the $BD+40°$ 4124 stellar cluster formed from a cloud-cloud collision. The largest linewidths occur near V1318 Cyg-S, a massive star affecting its natal environment. In contrast, the dense gas near the other, more evolved, massive stars displays no evidence for disruption; the material must either be processed into the star, dissipate, or relax, fairly quickly. The more evolved low-mass protostars are more likely to be found near the massive stars. If the majority of low-mass stars are coeval, the seemingly evolved low-mass protostars are not older: the massive stars have eroded their structures. Finally, at the highest resolution, the $\lambda = 3.1$ mm dust emission is resolved into a flattened structure 3100 by 1500 AU with an estimated mass of 3.4 $M_\odot$. The continuum and CS emission are offset by 1″1 from the southern binary source. A simple estimate of the extinction due to the continuum emission structure is $A_V \sim 700$ mag. From the offset and as the southern source is detected in the optical, the continuum emission is from a previously unknown very young, intermediate-mass, embedded stellar object.

[1]Department of Astronomy, University of Illinois, 1002 W. Green St., Urbana, IL 61801

[2]Department of Astronomy, University of Maryland, College Park, MD 20742

[3]Current Address: S & J Solutions LLC

[4]Max-Planck-Institut für extraterrestrische Physik, Garching, 85741, Germany

[5]Current Address: Department of Physics, University of California, Berkeley, CA

Subject headings: ISM: clouds—ISM: jets and outflows—radio lines: ISM—
stars: formation—stars: individual (BD + 40° 4124 , V1318 Cyg, V1318 Cyg-S,
V1318 Cyg-N)

1. Introduction

Over the last few decades, a good broad-brush picture of isolated, low-mass, Sun-like
star formation (e.g., Shu et al. 1993) has been developed. However, these theories are unlikely
to explain properly the formation of our Sun or indeed the majority of other stars in the
Galaxy. For our Sun in particular, the isotopic evidence strongly suggests that it formed in
a location that was enriched either by a stellar wind or a recent supernova (e.g., Lee et al.
1977), hence in or near a cluster environment. New results show that the early solar system
contained significant amounts of the short-lived ^{60}Fe radionuclide (e.g., Tachibana & Huss
2003), probably from a nearby supernova ($\sim$ 1.5 pc distance, Looney et al. 2006).

The suggestion that our Sun might have been born in a cluster environment, should
not be too surprising, as there is good evidence that the majority of stars in the Galaxy
formed in clusters (e.g., Carpenter 2000; Lada & Lada 2003). Giant molecular clouds in the
Galaxy provide the ideal environment for star formation, comprising dense molecular gas
and dust that provide the raw material (e.g. Zuckerman & Palmer 1974). But how do we
expect low-mass star formation to proceed in a cluster? According to the standard model
(e.g. Shu et al. 1987), it is a relatively long process requiring a core to exceed its Jeans mass,
initiate self-similar collapse, followed by multiple fragmentation down to star formation with
the Initial Mass Function (IMF) stellar distribution. In this model, higher mass stars form
quickly and low mass stars form slowly.

However, in clusters the environment is much more complicated. Clusters are often
associated with one or many massive stars accompanied by a large number of lower mass
stars. In fact, the typical star forming system is actually a low stellar density cluster,
including young intermediate to high mass star or stars (3-20 $M_\odot$) surrounded by ten to
a few hundred of low-mass protostars. This trend for massive stars to be more and more
gregarious, is first associated with stars at the Herbig Ae/Be stage (e.g. Hillenbrand et al.
1995; Palla et al. 1995). In such an environment, the standard model has to be modified for
the large influence that the massive star will have on low-mass star formation and evolution.
The low-mass star may evolve faster than in isolation. It has been posited that stellar
formation in a large cluster, with a combined mass of a few hundred $M_\odot$, evolves faster

by minimizing the effects of magnetic fields (Shu et al. 1987). Are low-mass stars formed coevally with massive stars during a trigger event? Are low-mass stars triggered by the high mass star?

In order to better understand the differences between isolated low-mass star formation and low-mass star formation in a cluster with massive stars, it is important to understand the most simple case of small clusters, or groups, around intermediate-mass stars. One of the main points is to develop a better picture of how the most massive members of the cluster influence the formation of the lower-mass members by probing the dense molecular gas, dust, and stellar population. An excellent example is the small cluster surrounding the intermediate-mass/massive ($\sim 9\ M_\odot$), young (~ 1 Myr; Hillenbrand et al. 1995) star BD + 40° 4124 , one of the original Ae/Be stars studied by Herbig (1960). Although the main star has a spectral type of B2 Ve and is hot enough ($T_{\mathrm{eff}} > 22\,000$ K), there is no observational evidence for an H II region (Skinner et al. 1993). Located in the Cygnus arm at a distance of about one kiloparsec, BD + 40° 4124 is the optically brightest member of a small group of young stars that include V1686 Cyg and the binary V1318 Cyg, all of which have infrared excesses (Strom et al. 1972) and are very young (Cohen 1972).

BD + 40° 4124 defines the center of a partially embedded aggregate of at least 33 stars, 80% of which are located within a projected distance of 0.15 pc from the central star (Hillenbrand et al. 1995). Single-dish maps of CO, ^{13}CO, C^{18}O and CS, (Hillenbrand et al. 1995; Palla et al. 1995) and NH$_3$ (Fuente et al. 1990), show that this relatively isolated and dense ($n \gtrsim 1000\,\mathrm{stars\,pc^{-3}}$) cluster is still associated with more than $\sim 300\ M_\odot$ of clumpy, dense molecular material. Therefore, ongoing star-formation is still possible in this region. In fact, Hillenbrand et al. (1995) concluded that high- and low-mass stars are still forming, with the balance in favor of high-mass stars.

This small and young group of stars is interesting for two main reasons. First, the parent molecular core is isolated from any large star-forming complex, and, therefore, this region is an ideal site to investigate the conditions in which a single high-mass star, capable of becoming a supernova ($M_* \gtrsim 8\,M_\odot$) forms, and its role, if any, in the formation of its lower-mass siblings. Second, Hillenbrand et al. (1995) concluded that star formation in this region was triggered by an external event, based on morphological arguments. However, no evidence can be found for any of the standard mechanisms for induced star formation (e.g. nearby expanding H II regions, supernova remnants, or nearby OB associations).

To unravel the star-formation history of this region it is first necessary to identify the sites of ongoing– and potentially future– star formation and to study the kinematic signatures and physical conditions of these sites. The observations focused on the CS ($2 \rightarrow 1$) transition, as a tracer of dense gas. Due to its high critical density, ($n_{H_2} \sim 10^5\,\mathrm{cm^{-3}}$, e.g. Irvine et al.

1987), CS $(2 \to 1)$ is thermalized in the dense gas of star-forming cores. In other words, CS emission is a good method for revealing dense, star forming clumps. To date, the available observations at millimeter wavelengths are of moderate spatial resolution– they were all obtained with single-dish telescopes. In this paper, we present high spatial- and spectral-resolution data obtained with the BIMA array in the $J = 2 \to 1$ transition of CS and dust continuum emission that probe the dense gas and dust in the young cluster on spatial scales of 1000's to 10,000's of AU.

2. Observations

BD + 40° 4124 was observed in three configurations (B, C, and D) of the 10-element BIMA Array[1] (Welch et al. 1996). The uncertainty in the absolute amplitude calibration is estimated to be 20%; all BIMA flux uncertainty discussed is the statistical uncertainty and does not account for any amplitude calibration error. The CS $J = 2 \to 1$ ($\nu = 97.981$ GHz) observations in B and D configurations were acquired in 2003 March and August. The digital correlator was configured with the line window having a velocity range of 69 km/s with 0.27 km/s channels and two 600 MHz bands for continuum. The system temperatures during the observations ranged from 170-600 K (Single Side-Band, SSB). In addition, we also used archival data from 1996 August of the 9-element array in C configuration. The digital correlator for the archival data was configured similarly but with only 500 MHz bands for continuum. The system temperatures for the archival data ranged from 310-500 K (SSB).

The data were reduced with the MIRIAD package (Sault et al. 1995). The observations span u,v distances from 2 kλ to 75 kλ, providing brightness distribution information on spatial scales from $40''$ to $1''1$. In order to display this information in the image plane, we mapped the data using all three configurations with two different u,v weighting schemes that stress structures on spatial scales of roughly $6''$ and $2''$. These resolutions were obtained with robust weighting (Briggs 1995) values of 0.2 and -0.5, respectively.

BD + 40° 4124 continuum submillimeter observations were obtained from the public archive data of the Submillimetre Common User Bolometer Array (SCUBA) instrument on the James Clerk Maxwell Telescope (JCMT). The observations were carried-out using the long wavelength array at 850 μm and the short wavelength array at 450 μm. The source was observed in 1997 September. The observing conditions were poor; the average sky opacities during the observation were $\tau_{850\mu m} = 0.91$ at 850 μm and $\tau_{450\mu m} = 5.19$ at 450 μm. The data were reduced using the SCUBA User Reduction Facility procedures (Jenness & Lightfoot 1998). Specific care was taken to remove sky noise and saturated bolometers. The planet Uranus and CRL 2688 were used as flux calibrators. The data were reduced for both long

and short wavelengths to ensure consistency, although only the long wavelength array data are used. An uncertainty in the absolute flux calibration as 20% is estimated; all SCUBA flux uncertainty discussed is the statistical uncertainty and does not account for any amplitude calibration error.

3.   Results

The BIMA data provide the highest resolution observations of dense gas in the BD + 40° 4124 cluster to date. The data were obtained in three configurations of the interferometer, each probing structure on varying size-scales. The data was combined and weighted to emphasize structures on two different size scales– $\sim 6''$ and $2''$, or equivalent to a spatial resolution of 6000 and 2000 AU, a good scale for finding low-mass multiple systems (Looney et al. 2000). Additionally, the interferometric data resolve out the very large-scale emission from the molecular core, allowing us to probe the localized density enhancements (Looney et al. 2003). Along with SCUBA dust continuum emission and infrared images, we can explore star formation toward BD + 40° 4124 by analyzing the dense molecular gas, dust, and stellar distribution.

3.1.   Dense Gas and Dust Morphology

Figure 1 illustrates the velocity-integrated maps of the CS (2-1) emission overlaid on an H-band adaptive optics observation of the core stellar components (Davies et al. 2001). One of the striking morphological features of the CS emission is the significant molecular gas along a ridge running nearly north-south with an extent of ~ 0.4 pc. This ridge of molecular emission is clearly aligned with the large amount of dust continuum emission detected in the JCMT SCUBA observations at $\lambda = 850$ μm (Figure 2). The two main peaks in the SCUBA image corresponds to the peaks labeled A and J in the CS maps. A comparison of the two maps shows that the CS emission is indeed tracing the densest regions, or the molecular cloud core. There are arguably 16 distinct clumps that can be recognized in the velocity integrated maps (Figures 1 & 2).

Figure 3 shows the corresponding dust continuum emission at $\lambda = 3.1$ mm for the

two resolutions. As for the case of the $\lambda = 850$ μm continuum, the two main peaks coincide with clumps A and J in the CS maps. At high-resolution, the bright peaks of the CS and continuum emission are centered near the close binary pair V1318, suggesting that this region is where the youngest members of the cluster are located. The two brightest stars in the H-band observation of Figure 1 (BD $+ 40°$ 4124 and V1686, spectral types B2 and B5, respectively) do not have any dense gas or dust associated with them: both are only at the edge of the CS emission. This fits in the picture that massive stars reveal themselves quickly. However, it is difficult to explain the lack of an H II region near BD $+ 40°$ 4124 if the star is ablating the edge of the dense gas.

3.2. Dust Structures

In Figure 3, the $\lambda = 3.1$ mm continuum emission (also detected by di Francesco et al. 1997, at lower resolution) is overlaid on the H-Band continuum. The low resolution image shows that many of the continuum peaks are cospatial with the CS peak emission. Under the assumption of optically thin, isothermal dust emission, the mass can be calculated using $F_\nu = B_\nu(T_{dust})\kappa_\nu M/D^2$. $B_\nu(T)$ is the Planck function, T_{dust} is the temperature of the dust, κ_ν is the dust mass opacity, M is the mass of gas and dust, and D is the distance to the source. Note that the derived mass scales roughly linear with the assumed dust temperature; we use $T_{dust} = 25$ K. For the dust mass opacity (e.g., Draine 1990; Pollack et al. 1994), we adopt a κ_ν which is consistent with other works (e.g., Beckwith & Sargent 1991; Looney et al. 2000): $\kappa_\nu = 0.1(\nu/1200$ GHz$)$ cm^2 g^{-1}, corresponding to $\kappa_\nu = 0.008$ cm^2 g^{-1} and $\kappa_\nu = 0.029$ cm^2 g^{-1} in the BIMA and SCUBA bands, respectively. Although we do not expect this simple model to give accurate masses, it provides rough estimates that are adequate for qualitative comparisons and are arguably within a factor of 2 of the likely total mass.

The two brightest continuum peaks in the low resolution image of Figure 3 are 48.2 $\pm$ 3.7 mJy and 17.6 $\pm$ 3.4 mJy. Using the above formalism, their estimated masses are 4.2 $M_\odot$ and 1.5 $M_\odot$, respectively. In the high resolution image the bright continuum emission peak is resolved and well fit as an extended Gaussian source of 3100 by 1500 AU, assuming a distance of 1 kpc, with a measured flux density of 38.6 $\pm$ 4.3 mJy, or a derived mass of 3.4 $M_\odot$. The extinction (A_V) at the center of the high resolution peak was derived by converting the peak brightness of 22.9 $\pm$ 1.8 mJy/beam into an H_2 column density. The mass in the peak beam is 2 $M_\odot$/beam. Using a hydrogen mass abundance ratio (X_H) of 0.7, that mass is equivalent to a column density of $N_{H_2} = 5.25\times 10^{23}$ cm^{-2} in the beam, again using a distance of 1 kpc. Assuming that $R_V = 3.2$, we can use the relationship $A_V / N(H_2) = 1.33 \times 10^{-21}$ cm^2 mag, after Bohlin et al. (1978). The extinction of the compact structure at the peak is $A_V \sim 700$

mag, a very dense region indeed.

Finally, the two brightest peaks in the SCUBA map (Figure 2) are 2.83 ± 0.045 Jy/Beam and 1.26 ± 0.045 Jy/Beam. An estimated point mass of 6.9 $M_\odot$ and 3.1 $M_\odot$, respectively, is determined. The total flux from the whole region is 28.2 ± 0.3 Jy, or 68.5 $M_\odot$, a factor of 4 less than the estimated molecular mass of the cloud from single-dish measurements. However, this mass estimate assumes a temperature of 25 K, which is probably an overestimate for the average temperature of the whole cloud, underestimating the total mass. In fact, a temperature estimate of 10 K for the whole region would match the mass of material detected in single dish observations– ~ 300 $M_\odot$.

3.3. Gas Kinematics

Sixteen locations (see Figure 2) were chosen based on the clumpiness of the CS emission in the low and high resolution integrated intensity maps. Figures 4 & 5 show the CS line emission integrated over a beam element at the 16 locations in the low and high resolution maps (see Figure 1), respectively. In general, the upper spectra are from the core region (containing the V1318 system) where the most active star formation is occurring, the middle spectra are from the northern spur, and the bottom spectra are from the fringe regions.

Table 1 lists the single Gaussian fits to the low spatial resolution spectra as labeled in Figure 2. There is a noticeable difference in the spectra when comparing the core region and the northern spur (also see Figure 6). First of all, the linewidths decrease from a maximum value of 2.78 km/s near the CS peak to 1.07 km/s at the northern clump K. In general, the linewidth generally decreases as the distance from the central core. Secondly, there are two clear linear correlations in the fitted Gaussian center velocity of the line. In the core (approximately -40″to 15″), the velocities increase from 7.2 km/s to 8.3 km/s, and in the northern spur (approximately 0″to 55″), again the velocities generally increase from 6.7 km/s to 7.5 km/s.

What is causing the two systematic velocity trends? One possibility is an overall rotation of the initial molecular cloud that formed the cluster, but there are two separate linear correlations in Figure 6. Another possibility is that the emission from the Northern component velocities are contaminated by outflows. However, at the highest resolution, where the line profiles are less influenced by outflow emission, the peak velocities are not significantly different (Figure 5). Finally, the most compelling argument is that the velocity gradients are real and that the elongated cloud consists of two components.

Indeed, the kinematics clearly suggest that the molecular material surrounding the

cluster consists of two clouds and that the systematic velocity gradients are due to rotation. The clumps P, O, N, C, A, B belong to cloud 1 and the clumps G, H, I, J, K, L to cloud 2. Assuming a rigid rotation cloud model, linear fits of the velocities over the offsets yield gradients of 0.033 and 0.015 km/s/$''$ for cloud 1 and cloud 2, respectively. The linear fit describes the data well for both clouds, as the scatter (RMS) of the residual are about 0.1 km/s compared to the initial scatter of 0.38 and 0.32 km/s, respectively. The clumps E and F are associated to cloud 1 as their velocities match the other clumps, but are excluded from the fit as they are spatially separated from the rest of cloud 1 and projection effects may place them at unsuitable offsets.

The evidence of two kinematically separate clouds implies that the northern spur is the remnant of a cloud that collided with the southern condensation. This is a very intriguing result, as these two clouds may be the remnant signature of the, so far, unknown trigger of star formation and account for its high star-formation efficiency. This may be compared to the recent ideas on the creation of molecular clouds from colliding streams of atomic hydrogen (e.g., Vázquez-Semadeni et al. 2003; Heitsch et al. 2005), but the material (CS compared to hydrogen), size-scales, and probable velocity linewidths are very different.

In addition to the collision of two clouds, there is a clear distinction in Figure 6 around the immediate region of clump A– the most active region of star formation in the cluster. The increased linewidths of the region, coupled with possible fluctuations in the peak velocities (i.e. clumps E and F), are arguably the effect of star formation in the V1318 Cyg region; an intermediate star churning up the intragroup environment with winds and outflows (see the following section). On the other hand, the dense gas nearest BD+40°4124 and V1686 Cyg displays no evidence of disruption, indicating that the disturbed material is processed quickly into the star, removed from the system, or relaxes fairly quickly.

There are two spectra that are not well fit by the Gaussian models in Figure 4 – clumps D and M. Because of this, they were not included in the above discussion. In the case of D, it is unclear if the dip in the center is from self-absorption or from two separate clumps. However, due to the unusual velocities for the two clumps and the reduction in brightness compared to the other central regions, we prefer the self-absorption scenario. There is a slight blue asymmetry to the emission that may be an indication of an infall signature from an embedded object (e.g. Walker et al. 1994). However, at high resolution (Figure 5) only the blue component is observed. Also, as seen in Figure 2, there is an extension in the submillimeter continuum toward clump D that has no stellar sources, perhaps indicating a region of dense material. For clump M, the spectra clearly show the classical signature of a P-Cygni profile. Clump M may be affected by the Herbig Ae/Be source V1686 Cyg. If this interpretation is correct, the line is absorbing against the large-scale continuum; there

is no detected compact emission by the interferometer, but the large continuum source (e.g. Figure 2) is resolved out.

3.4.   Outflow Feature

In Figure 4, one can distinguish components from an outflow at 4 km/s and 11 km/s. Figure 7 shows the velocity integrated emission over the blue (2.462 - 4.854 km/s) and red components (10.236 - 12.03 km/s) of the clump A wings. This is consistent with the emission being the low-velocity dense component of the detected large-scale outflow detected in CO (Palla et al. 1995). It is also interesting to note that the source of the outflow is better attributed to the maser object than the optical/IR southern binary (Figure 3, high resolution).

3.5.   Column Densities and Masses of the Clumps

From the observation of a single transition, the total number density, n_{H_2}, and kinetic temperature, T_K, of the emitting region can not be derived. However, the *range* of molecular column densities that can account for the observed brightness temperatures can be estimated. By computing a grid of Large-Velocity-Gradient (LVG) models with a range of n_{H_2}, T_K, and molecular column densities N_{CS} as input, and using this grid to fit the observed brightness temperatures, a range of N_{CS} is found that can account for the emission. The usefulness of the obtained molecular column densities depends on the range limits. Note that, because only one transition is at hand, only one of n_{H_2}, T_K, or N_{CS} can be deduced in this manner. N_{CS} is chosen, as the amount of molecular gas is particularly interesting and the range in N_{CS}, consistent with the observed emission, is always narrower than the corresponding ranges in T_K and n_{H_2}.

The output range of N_{CS} can be narrowed further by considering only those models for which the optical depth of the transition under consideration is $\lesssim 2$. This constraint is based on the fact that for $\tau \gtrsim 2$ the validity of the LVG approximation is uncertain– at best. In the case at hand, the observations of Fuente et al. (1990) provide an additional constraint. They deduced T_K from the (1,1) and (2,2) lines of NH_3, and found values ranging from 18 K to 27 K. Therefore, the input values of T_K can be chosen to be in the range 15–30 K.

A grid of LVG models was computed with 9 kinetic temperatures in the range 10–100 K, 9 values of n_{H_2} in the range 10^4–10^8 cm^{-3}, and 20 CS column densities in the range 10^{13}–10^{15} cm^{-3}– logarithmically spaced in all three variables. The obtained values of N_{CS}

(for $15K \leq T_K \leq 30K$ and $\tau \leq 2$; and using the values of Δv_{FWHM} and their uncertainties in Table 1 are presented in Table 2.

With this range of N_{CS} and assuming $X_{CS} = 10^{-9}$ for the CS to H_2 abundance, the mass range of the clumps (Table 2) were deduced from

$$M = \mu m_H \frac{N_{CS}}{X_{CS}} \left(1.13\,\theta_a\theta_b D^2\right) \tag{1}$$

where $\mu = 2.33$ is the mean molecular weight, m_H is the mass of the hydrogen atom, and the last term is the area subtended by the beam at a distance D (1 kpc). This can be compared to the virial mass as calculated from

$$M_{\rm vir} = \frac{5}{3} \left(\frac{3}{8\ln 2}\right)^{1/2} \frac{\Delta v_{FWHM}^2}{G} R, \tag{2}$$

where R is the physical radius subtended by the beam.

Perusal of Table 2 shows that, for each emission peak, the range of N_{CS} is fairly narrow and the typical column density of H_2 is $\lesssim 10^{23}$ cm^{-2}, consistent with our estimate from the continuum data. It is not surprising that the column densities are an order of magnitude larger than that derived from single dish ^{13}CO data (Cantó et al. 1984) and a factor of two larger than the single dish value estimated using ^{12}CO and ^{13}CO (Hillenbrand et al. 1995). The higher spatial resolution of interferometric observations, 6″ compared to 66″ and 15″ for Cantó et al. (1984) and Hillenbrand et al. (1995), respectively, allow the distinction of high density clumps and not averaging them out. However, it is important to note that the molecular hydrogen column densities presented on Table 2 were derived assuming a CS to H_2 abundance of 10^{-9}, which could be too large by a factor ~ 5.

Finally, comparison of the masses derived from the LVG analysis and those computed with the virial theorem show that in all cases $M < M_{\rm vir}$. Given the crudeness of the LVG analysis presented here, it is difficult to draw any definitive conclusion from this result.

3.6. Stellar Population

Figures 1, 2, and 3 also show the distribution of the known stellar population (Hillenbrand et al. 1995, although the observations were not deep: 100% complete at K=15.3) with respect to the dust and dense gas. The star symbols are IR sources with optical counterparts while the triangles are IR sources without any known optical counterparts. IR excesses are found in 100% of the known stellar population (Hillenbrand et al. 1995); both the low-mass and the high-mass stars are young. This suggests that low-mass and high-mass star formation occurred quickly– < 1 Myrs with high formation efficiency.

However, the evolutionary stages of the sources are difficult to estimate until more is known about their spectral energy distributions and the foreground extinction. Nonetheless, one can compare the extinction of the sources estimated from their position on a color-magnitude diagram (e.g. Figure 8 in Hillenbrand et al. 1995) to the extinction estimated from the CS line. The estimated extinction in the clumps range from $A_V = 14$ to > 100 mag on the molecular ridge of material. For the optically visible IR sources in Figure 1, the extinctions are typically around $A_V \sim 1$ regardless of location– on-ridge or off-ridge. The major exception is V1686 Cyg, which has a high extinction estimate (Hillenbrand et al. 1995) and is near the molecular ridge. Similarly, the majority of the IR sources without optical counterparts have extinctions that are typically around $A_V \sim 13$. As the extinction is independent of the source field position, the effect is probably due to local conditions at the source, not its location within the dense molecular gas. In general, this evidence leads to the assumption that typically, the IR only sources are slightly embedded protostars (i.e. Class I/II) while the optically visible sources are young stars similar to T Tauri systems (i.e. Class II/III).

In that case, 19 out of a total of 31 stars in our field (7/10 of the Class II/III objects and 12/21 of the Class I/II objects) are closely associated with dense gas. It can be argued that the majority of the protostars are very closely associated with the CS ridge and that the Class II/III sources are forming closer to the more massive stars, neglecting projection effects. If star formation started approximately coevally, this suggests that the massive stars hasten the evolution of the objects nearest them. In other words, the massive stars reveal the low-mass stars from their dust cocoons, making them appear more evolved. On the other hand, as the ridge of intracluster material is clumpy on the size-scale expected for protostellar cores, many of the numerous dense gas clumps in Figure 1 may be harboring deeply embedded stellar counterparts. For example, a low-mass Class 0 system would not be seen in the IR as the dense envelope extincts light at wavelengths less than 10 μm. Indeed, in this paper we will show evidence for an intermediate-mass deeply embedded protostar; future FIR observations will help identify other such embedded objects. Star formation is not completely coeval in this region.

Finally, it is clear that the IMF of this cluster is unusually top-heavy based on the known star counts (Hillenbrand et al. 1995). Does the IMF vary locally with an integrated value over clusters? Or is the hidden population of low-mass stars enough to compensate. A census of the hidden low-mass stellar population would be extremely helpful. Indeed, this may be addressed with Spitzer observations of this region.

4.   A New, Deeply Embedded Protostar

The resolved dust structure in Figure 3 could be a flattened circumstellar disk, but we suggest that, due to its size, this structure is more likely a flattened envelope that surrounds a protostar; in particular, an unknown deeply embedded intermediate mass protostar. As seen in the zoomed inlay of Figure 3, the peak of the dust emission is offset by $1\rlap{.}''1$ to the northeast from the southern member of the V1318 binary. This offset is inconsistent with the observational uncertainties (expect $\sim 0\rlap{.}''5$). In addition, this location is precisely where H_2 emission is detected (Davies et al. 2001) and is coincident within $\sim 0\rlap{.}''25$ of the recent water maser emission observations (the square symbol in Figure 3, Marvel 2006). The high resolution ($\sim 2''$) CS emission shown in Figure 1 also has an offset similar to the continuum. In fact, although it can not be ruled out by these data alone, if the continuum and its associated extinction ($A_V \sim 700$) is physically associated with the southern source, i.e. the extinction is due to the massive envelope of the embedded objects, we must have a unique geometric observing position to detect the southern binary object in the optical at all. Rather, due to the discussion above, we suggest that the compact continuum emission and high resolution CS emission are actually tracing a younger, more embedded object, probably an intermediate-mass protostar. Indeed, a young cluster population appears to be lurking inside the dense gas. The southern component of the binary, must be a star at an older stage of evolution at an unfortunate projection.

5.   Conclusions

In this paper, we have probed the dense gas and dust in the small cluster associated with the intermediate-mass young star $BD + 40° 4124$. The dense gas, as traced by CS J = $2 \rightarrow 1$, consists of ~ 16 clumps that have the morphology of a dense molecular ridge about ~ 0.4 pc in size. By a simple LVG analysis of the clumps, we find that the typical estimated mass of the clumps is ~ 0.5 $M_\odot$. Although it is impossible with this data to predict which, if any, of these clumps may contain a young, deeply embedded population of protostars, it seems likely that some clumps do.

In particular, we resolve a flattened dust structure, 3100×1500 AU in size that is $1.1''$ offset from the southern component of the V1318 Cyg binary system, but well aligned with the water maser position. By modeling the circumstellar emission as arising from optically thin isothermal dust, a mass of 3.4 $M_\odot$ is estimated for the structure. The V1318 Cyg binary system is optically visible; however, the extinction is expected to be around $A_V \sim 700$ mag. With so high an extinction, the central source should not be visible. If the optically visible V1318 S is the source of the continuum emission, it would require an unusual geometry

that is not evident in the continuum emission. Based on the offset and the visibility of V1318 Cyg-S, we suggest that this object is a hereto unknown young embedded object and not V1318 Cyg-S. The structure, based on its mass, is probably a flattened circumstellar envelope which contains an intermediate mass, deeply embedded protostar. Indeed, star formation is still ongoing in this cluster.

However, we posit that, in general, star formation of this small cluster was coevally triggered by the collision of two clouds. The dense gas detected in this paper is essentially the remnants of the two original cores. The main reason for this conclusion is that the systematic velocity of the CS $(2 \rightarrow 1)$ transition suggests the presence of two independently rotating clouds, distributed spatially: cloud 1 is the center of the southern star forming activity and cloud 2 is the northern spur. Currently, cloud 1 is the center of the dense dust and gas in the cluster. Triggered star formation would probably explain the high star formation efficiency in the system.

Finally, there is evidence, e.g. the linewidths of the V1318 Cyg region, that the young intermediate mass stars in the core are disrupting the dense gas, which interferes with coeval lower-mass star formation. However, it must also be noted that this argument also implies that the previous stages of star formation, in particular the formation of $BD + 40° 4124$ and V1686 Cyg, did not disrupt the kinematics of the residual clouds significantly. In other words, the gas that was affected by their formation has been processed into the star, removed from the system, or relaxed fairly quickly. Another example of this is that the more evolved low-mass protostars are more likely to be near the more massive young stars. If the system was triggered by colliding clouds, then the majority of the low-mass stars are of similar ages. That implies that the presences of the higher mass protostars either hastens the lower-mass evolution, or that the more massive stars oblate the circumstellar structures of the lower-mass siblings, making them appear older.

REFERENCES

Beckwith, S. V. W. & Sargent, A. I. 1991, ApJ, 381, 250

Bohlin, R. C., Savage, B. D., & Drake, J. F. 1978, ApJ, 224, 132

Briggs, D. S. 1995, Bulletin of the American Astronomical Society, 27, 1444

Cantó, J., Rodriguez, L. F., Calvet, N., & Levreault, R. M. 1984, ApJ, 282, 631

Carpenter, J. M. 2000, AJ, 120, 3139

Cohen, M. 1972, ApJ, 173, L61

Davies, R. I., Tecza, M., Looney, L. W., Eisenhauer, F., Tacconi-Garman, L. E., Thatte, N., Ott, T., Rabien, S., Hippler, S., & Kasper, M. 2001, ApJ, 552, 692

di Francesco, J., Evans, N. J., Harvey, P. M., Mundy, L. G., Guilloteau, S., & Chandler, C. J. 1997, ApJ, 482, 433

Draine, B. T. 1990, in ASP Conf. Ser. 12: The Evolution of the Interstellar Medium, 193–205

Fuente, A., Martin-Pintado, J., Bachiller, R., & Cernicharo, J. 1990, A&A, 237, 471

Heitsch, F., Burkert, A., Hartmann, L. W., Slyz, A. D., & Devriendt, J. E. G. 2005, ApJ, 633, L113

Herbig, G. H. 1960, ApJS, 4, 337

Hillenbrand, L. A., Meyer, M. R., Strom, S. E., & Skrutskie, M. F. 1995, AJ, 109, 280

Irvine, W. M., Goldsmith, P. F., & Hjalmarson, A. 1987, in ASSL Vol. 134: Interstellar Processes, 561–609

Jenness, T. & Lightfoot, J. F. 1998, in ASP Conf. Ser. 145: Astronomical Data Analysis Software and Systems VII, 216–+

Lada, C. J. & Lada, E. A. 2003, ARA&A, 41, 57

Lee, T., Papanastassiou, D. A., & Wasserburg, G. J. 1977, ApJ, 211, L107

Looney, L. W., Mundy, L. G., & Welch, W. J. 2000, ApJ, 529, 477

—. 2003, ApJ, 592, 255

Looney, L. W., Tobin, J. J., & Fields, B. D. 2006, ApJ submitted

Loren, R. B. 1977, ApJ, 218, 716

Marvel, K. B. 2006, ApJ submitted

Palla, F., Testi, L., Hunter, T. R., Taylor, G. B., Prusti, T., Felli, M., Natta, A., & Stanga, R. M. 1995, A&A, 293, 521

Pollack, J. B., Hollenbach, D., Beckwith, S., Simonelli, D. P., Roush, T., & Fong, W. 1994, ApJ, 421, 615

Sault, R. J., Teuben, P. J., & Wright, M. C. H. 1995, in ASP Conf. Ser. 77: Astronomical Data Analysis Software and Systems IV, 433–+

Shu, F., Najita, J., Galli, D., Ostriker, E., & Lizano, S. 1993, in Protostars and Planets III, 3–42937

Shu, F. H., Adams, F. C., & Lizano, S. 1987, ARA&A, 25, 23

Skinner, S. L., Brown, A., & Stewart, R. T. 1993, ApJS, 87, 217

Strom, K. M., Strom, S. E., Breger, M., Brooke, A. L., Yost, J., Grasdalen, G., & Carrasco, L. 1972, ApJ, 173, L65+

Tachibana, S. & Huss, G. R. 2003, ApJ, 588, L41

Vázquez-Semadeni, E., Ballesteros-Paredes, J., & Klessen, R. S. 2003, ApJ, 585, L131

Walker, C. K., Narayanan, G., & Boss, A. P. 1994, ApJ, 431, 767

Welch, W. J., Thornton, D. D., Plambeck, R. L., Wright, M. C. H., Lugten, J., Urry, L., Fleming, M., Hoffman, W., Hudson, J., Lum, W. T., Forster, J. . R., Thatte, N., Zhang, X., Zivanovic, S., Snyder, L., Crutcher, R., Lo, K. Y., Wakker, B., Stupar, M., Sault, R., Miao, Y., Rao, R., Wan, K., Dickel, H. R., Blitz, L., Vogel, S. N., Mundy, L., Erickson, W., Teuben, P. J., Morgan, J., Helfer, T., Looney, L., de Gues, E., Grossman, A., Howe, J. E., Pound, M., & Regan, M. 1996, PASP, 108, 93

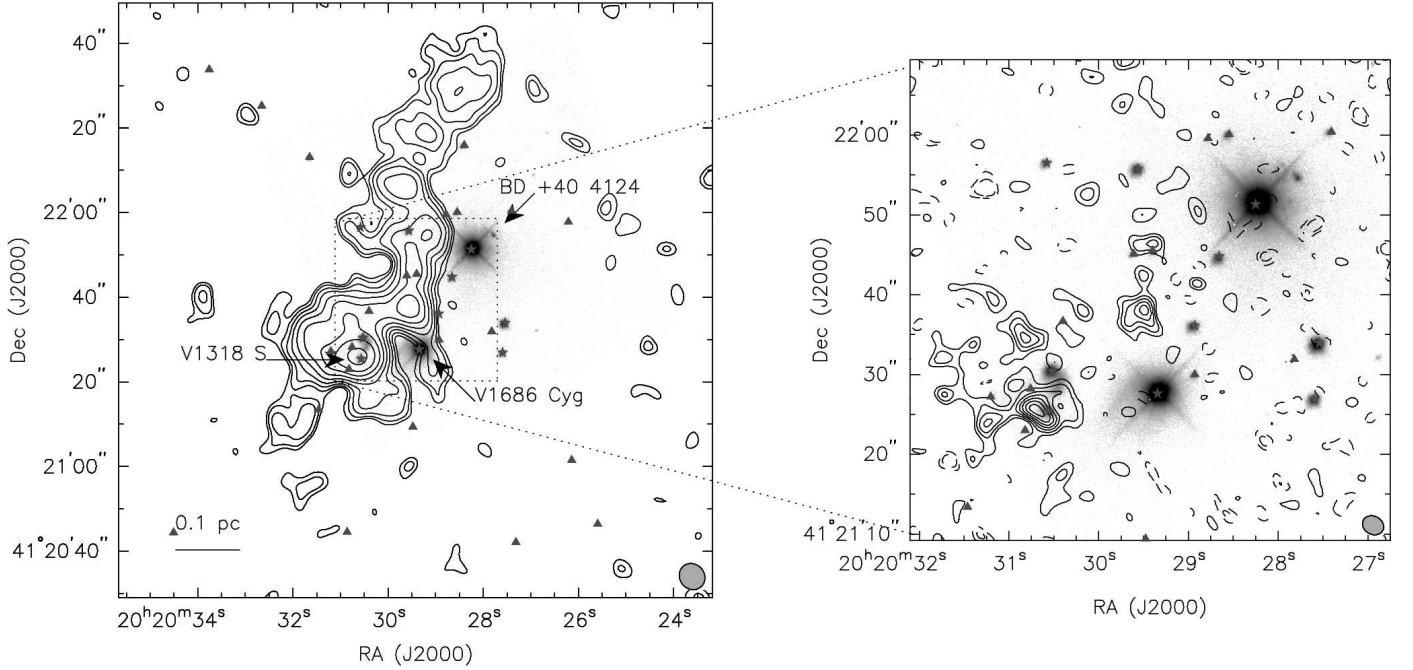Zuckerman, B. & Palmer, P. 1974, ARA&A, 12, 279

Fig. 1.— CS (2-1) emission toward the BD + 40° 4124 young cluster overlaid on a smaller adaptive optic H-Band image (Davies et al. 2001). Both CS maps are made from the same data with different weighting. On the left is the low resolution image emphasizing the large-scale structures. The noise is 0.2 Jy/beam km/s. The contours are logarithmically spaced (increment $\sqrt{2}$) from 2 to 64 times the noise. The negative contours, presumably from resolved out large-scale emission, are not shown to simplify the image. The beam, shown in the lower-right corner, is $6''\!\!.42 \times 5''\!\!.83$ with a PA of 40°. The dotted box indicates the zoomed field of the high resolution map (right). The high resolution image emphasizes the smaller-scale clumps of material traced by CS. The noise is 0.29 Jy/beam km/s. The contours are linearly spaced from 2 to 7 (positive and negative) times the noise. The beam, shown in the lower-right corner, is $2''\!\!.76 \times 2''\!\!.27$ with a PA of 62°. The symbols indicate IR sources: the star symbols indicate IR sources with optical counterparts, and the triangle symbols indicate IR sources without an optical counterpart (presumably more embedded objects, thus younger).
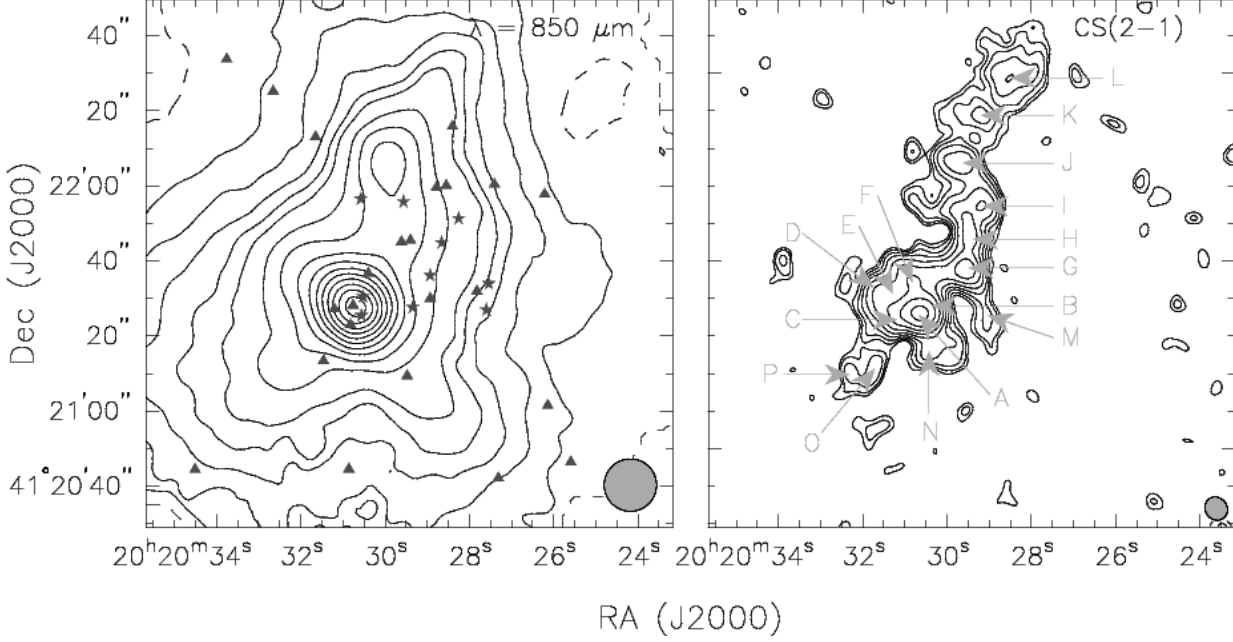
Fig. 2.— $\lambda = 850\ \mu$m continuum emission toward the BD $+ 40°$ 4124 young cluster in the left panel is archival SCUBA observations. The contours are in steps of 2 from 2 to 10 and in steps of 5 from 10 to 60 times the noise of 0.045 Jy/beam. The beam shown at the lower right is 14.7″. The symbols are the same as in Figure 1. The right panel is the low resolution CS emission from Figure 1 with the 16 clumps labeled.
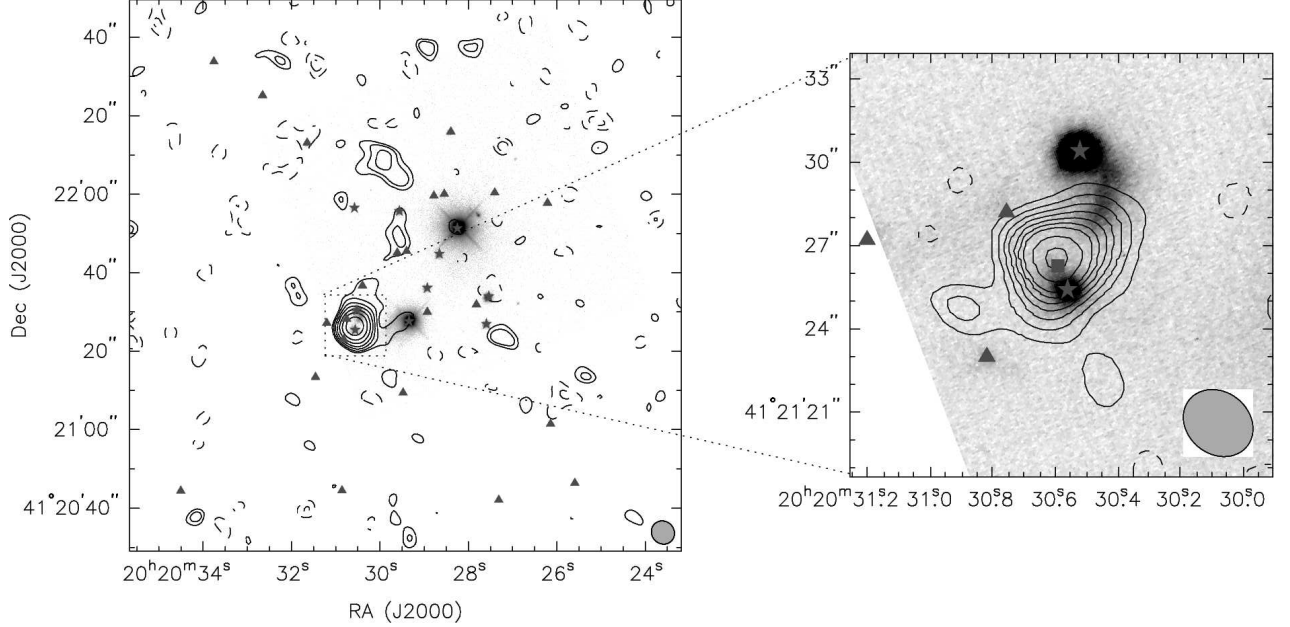
Fig. 3.— $\lambda = 3.1$ mm continuum emission toward the BD + 40° 4124 young cluster overlaid on a smaller adaptive optic H-Band image (Davies et al. 2001). Both maps are made from the same data with different weighting. On the left is the low resolution image emphasizing the large-scale structures. The noise is 1.6 mJy/beam. The contours are logarithmically spaced (increment $\sqrt{2}$) from 2 to 32 times the noise; negative values are indicated by dashed contours. The beam, shown in the lower-right corner, is $6\rlap{.}{''}12 \times 5\rlap{.}{''}68$ with a PA of 45°. The dotted box indicates the zoomed field of the high resolution map (right). The high resolution image emphasizes the compact emission. The noise is 1.8 mJy/beam. The contours are linearly spaced from 2 to 20 (positive and negative in steps of two) times the noise. The beam, shown in the lower-right corner, is $2\rlap{.}{''}67 \times 2\rlap{.}{''}24$ with a PA of 52°. The triangle and star symbols are the same as in Figure 1, but the solid square indicates the position of the VLBA water maser source. Inset is a zoom of the V1318 region using a different colormap on the H-band data to emphasize the diffuse structure. Note that the H Band spur off the northern component is a real scattered light feature.
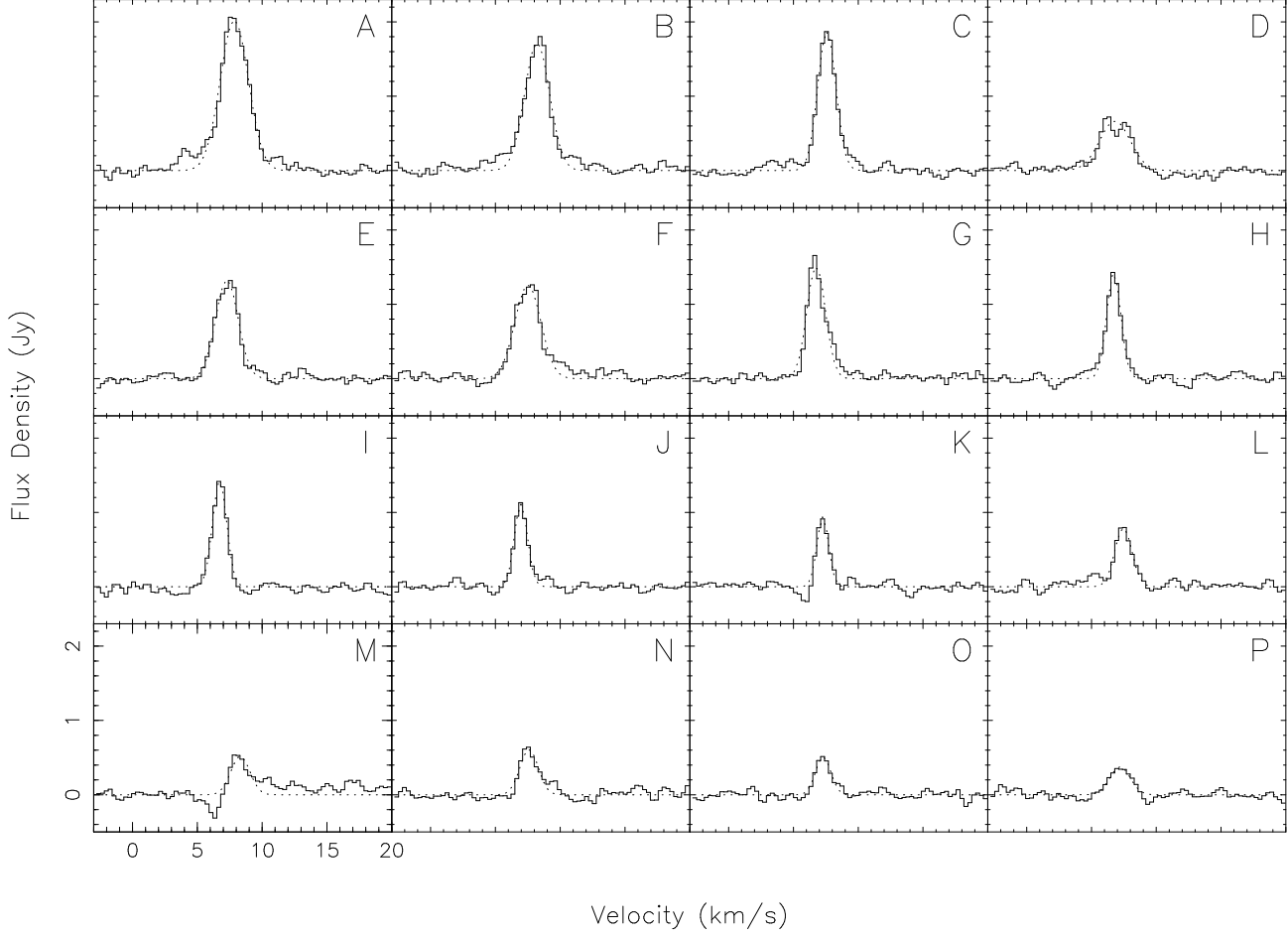
Fig. 4.— Beam averaged spectra of the 16 clumps in the low resolution image. The dashed line is the best fit Gaussian in each case, as labeled in Table 1.
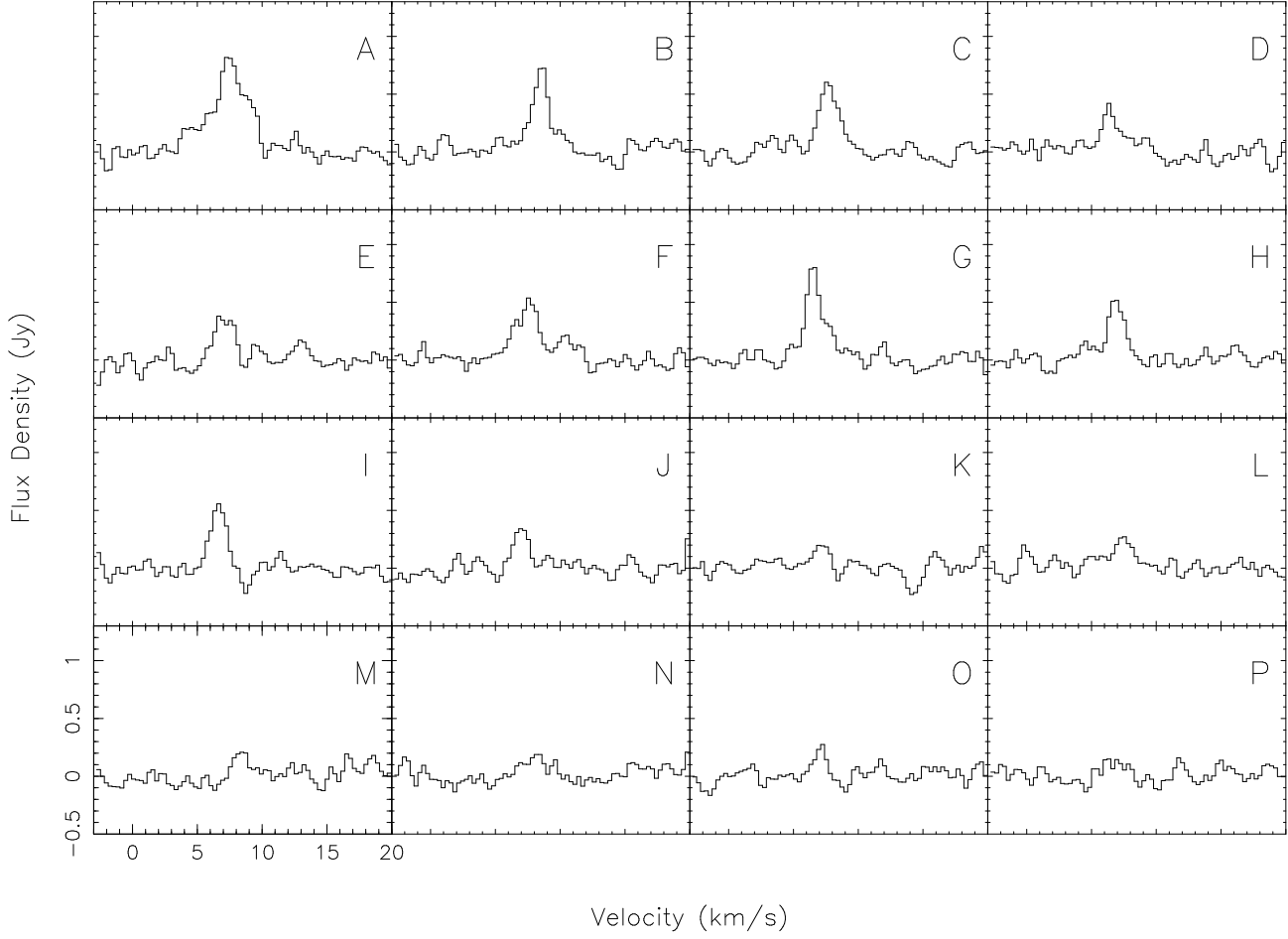
Fig. 5.— Beam averaged spectra of the 16 clumps in the high resolution image.
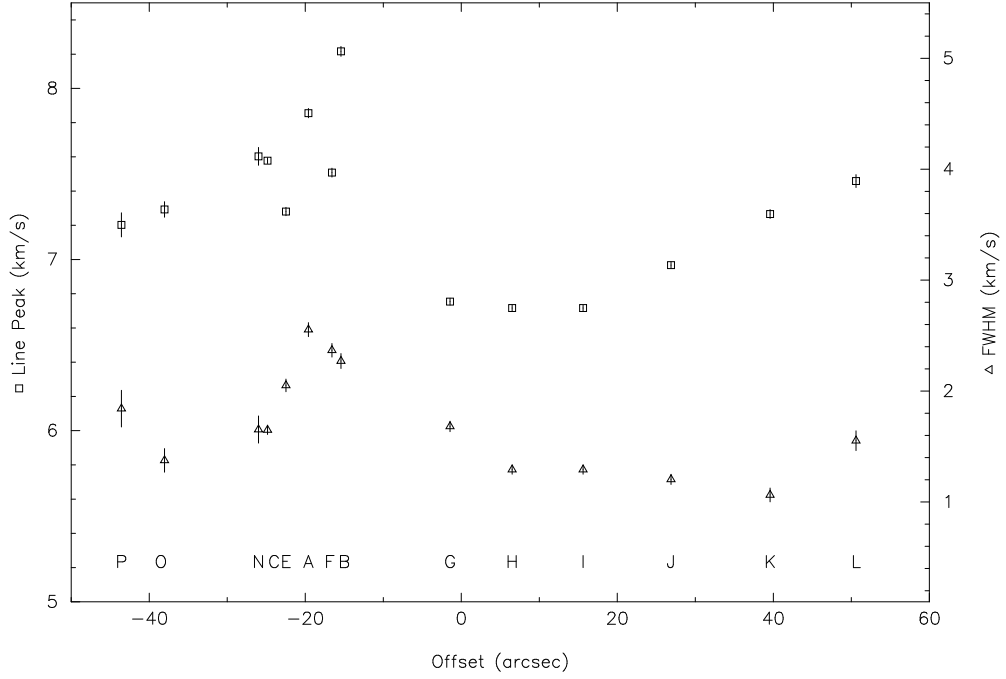
Fig. 6.— Comparison of the low resolution spectra peak velocity and linewidth with offset from the pointing center (near peak G) in arcseconds. Clumps D and M are not plotted as their Gaussian fits are not acceptable. The square symbols are the line center velocities of the remaining 14 best fit Gaussians, as indicated by the left-hand axis. The triangle symbols are the corresponding FWHM of the best fit Gaussians, as indicated by the right-hand axis. The error bars are the Gaussian fit error on the parameters. This assumes that the spectra are well defined as Gaussians. At the bottom, each clump is labeled with the associated letter.
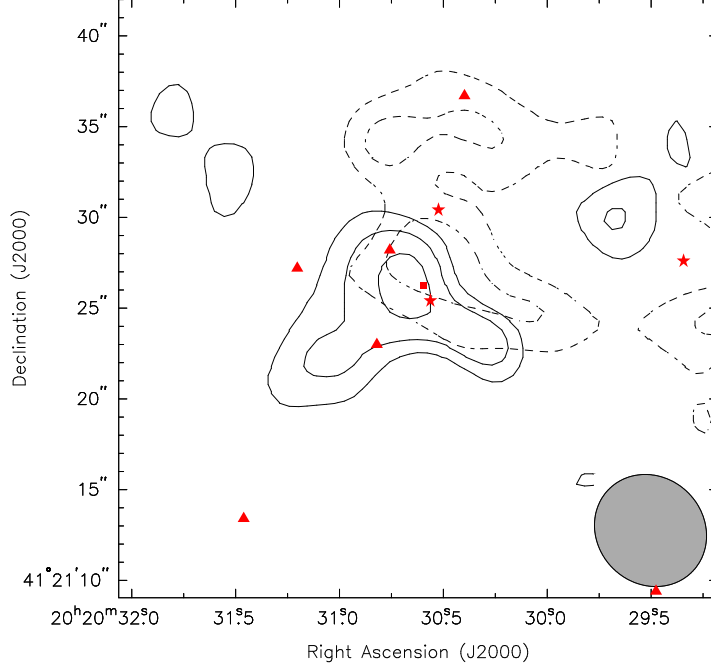
Fig. 7.— CS (2-1) emission toward the BD + 40° 4124 young cluster in the excess velocities of clump A (Figure 4). The velocity range of 2.462 - 4.854 km/s is the blue component (solid contours) and the velocity range of 10.236 - 12.03 km/s is the red component (dashed contours). The noise is 0.12 Jy/beam km/s. The contours are 2, 3, and 4 times the noise. The beam, shown in the lower-right corner, is 6$\farcs$42 × 5$\farcs$83 with a PA of 40°. The triangle and star symbols are the same as in Figure 1, but the solid square indicates the position of the VLBA water maser source.

Table 1.   Fit Parameters

Label	Position ″	Peak Jy	velocity km/s	FWHM km/s
A	-19.6	2.03 ± 0.04	7.86 ± 0.03	2.55 ± 0.07
B	-15.4	1.72 ± 0.04	8.22 ± 0.03	2.26 ± 0.07
C	-24.8	1.87 ± 0.04	7.58 ± 0.02	1.65 ± 0.03
D	-26.8	0.66 ± 0.03	6.81 ± 0.06	2.78 ± 0.15
E	-22.5	1.33 ± 0.03	7.28 ± 0.02	2.05 ± 0.05
F	-16.6	1.26 ± 0.05	7.51 ± 0.03	2.36 ± 0.07
G	-1.4	1.52 ± 0.04	6.75 ± 0.02	1.66 ± 0.05
H	6.5	1.43 ± 0.04	6.72 ± 0.02	1.30 ± 0.07
I	15.6	1.43 ± 0.04	6.72 ± 0.02	1.30 ± 0.07
J	26.9	1.11 ± 0.04	6.97 ± 0.02	1.20 ± 0.05
K	39.6	0.94 ± 0.05	7.27 ± 0.03	1.07 ± 0.07
L	50.6	0.79 ± 0.04	7.46 ± 0.04	1.55 ± 0.08
M	-14.5	0.52 ± 0.06	8.32 ± 0.10	1.71 ± 0.23
N	-26.0	0.61 ± 0.04	7.60 ± 0.05	1.65 ± 0.12
O	-38.0	0.51 ± 0.03	7.29 ± 0.03	1.38 ± 0.10
P	-43.6	0.38 ± 0.03	7.20 ± 0.07	1.85 ± 0.17

Table 2.   Derived Column Densities and Masses

Position	N_{CS} $\log(\mathrm{cm}^{-2})$	N_{H_2} $\log(\mathrm{cm}^{-2})$	M $M_\odot$	M_v $M_\odot$
A	13.41-14.14	22.41-23.14	0.33-1.80	26.9
B	13.35-14.09	22.35-23.09	0.29-1.58	21.2
C	13.22-13.95	22.22-22.95	0.21-1.15	11.3
D†	13.44-13.87	22.44-22.87	0.36-0.95	32.0
E	13.31-13.52	22.31-22.52	0.26-0.42	17.4
F	13.37-13.90	22.37-22.90	0.30-1.01	23.1
G	13.22-13.85	22.22-22.85	0.21-0.90	11.4
H	13.11-13.75	22.11-22.75	0.17-0.73	7.0
I	13.11-13.75	22.11-22.75	0.17-0.73	7.0
J	13.08-13.50	22.08-22.50	0.15-0.40	6.0
K	13.03-13.45	22.03-22.45	0.14-0.40	4.7
L	13.19-13.61	22.19-22.61	0.20-0.53	10.0
M†	13.23-13.55	22.23-22.55	0.22-0.46	12.1
N	13.22-13.64	22.22-22.64	0.21-0.55	11.3
O	13.14-13.46	22.14-22.46	0.18-0.37	7.9
P	13.27-13.48	22.27-22.48	0.24-0.39	14.2

†Note that the derived masses of D and M may not be valid if the J=2-1 CS line is self-absorbed ($\tau > 2$).